MXene coupled graphitic carbon nitride nanosheets based plasmonic photocatalysts for removal of pharmaceutical pollutant

Ajay Kumar [a,1], Palak Majithia [a], Priyanka Choudhary [a], Ian Mabbett [b], Moritz F. Kuehnel [b,c], Sudhagar Pitchaimuthu [d,e], Venkata Krishnan [a,*]

[a] School of Chemical Sciences and Advanced Materials Research Center, Indian Institute of Technology Mandi, Kamand, Mandi, 175075, Himachal Pradesh, India
[b] Department of Chemistry, Swansea University, Singleton Park, Swansea, SA2 8PP, Wales, United Kingdom
[c] Fraunhofer Institute for Wind Energy Systems IWES, Am Haupttor 4310, 06237, Leuna, Germany
[d] SPECIFIC, College of Engineering, Swansea University (Bay Campus), Swansea, SA1 8EN, Wales, United Kingdom
[e] Research Centre for Carbon Solutions, Institute of Mechanical, Process and Energy Engineering, School of Engineering and Physical Sciences, Heriot-Watt University, Edinburgh, EH14 4AS, United Kingdom

HIGHLIGHTS

- Plasmonic photocatalyst comprising g-C_3N_4, Ti_3C_2 MXene and Au NP was prepared.
- Photocatalyst was used for degradation of a pharmaceutical pollutant cefixime.
- Optimized loading of MXene in photocatalyst leads to remarkable activity.
- Mechanistic investigation of catalytic activity of novel ternary photocatalyst.

GRAPHICAL ABSTRACT
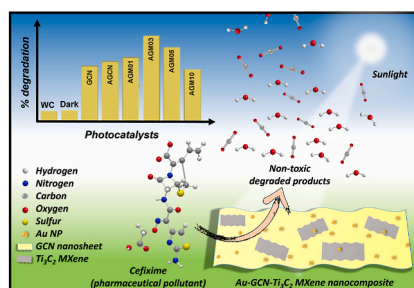
ARTICLE INFO

ABSTRACT

The continuous rise in the amount of industrial and pharmaceutical waste in water sources is an alarming concern. Effective strategies should be developed for the treatment of pharmaceutical industrial waste. Hence the alternative renewable source of energy, such as solar energy, should be utilized for a sustainable future. Herein, a series of Au plasmonic nanoparticle decorated ternary photocatalysts comprising graphitic carbon nitride and Ti_3C_2 MXene has been designed to degrade colourless pharmaceutical pollutants, cefixime under visible light irradiation. These photocatalysts were synthesized by varying the amount of Ti_3C_2 MXene, and their catalytic potential was explored. The optimized photocatalyst having 3 wt% Ti_3C_2 MXene achieved 64.69% removal of the pharmaceutical pollutant, cefixime within 105 min of exposure to visible light. The presence of the Au nanoparticles and MXene in the nanocomposite facilitates the excellent charge carrier separation and increased the number of active sites due to the formation of interfacial contact with graphitic carbon nitride nanosheets. Besides, the plasmonic effect of the Au nanoparticles improves the absorption of light causing enhanced photocatalytic performance of the nanocomposite. Based on the obtained results, a plausible mechanism has been formulated to understand the contribution of different components in photocatalytic activity. In addition, the

* Corresponding author.
  E-mail address: vkn@iitmandi.ac.in (V. Krishnan).
[1] Current address: School of Engineering and Innovation, The Open University, Milton Keynes, MK76AA, United Kingdom.

optimized photocatalyst shows excellent activity and can be reused for up to three cycles without any significant loss in its photocatalytic performance. Overall, the current work provides deeper physical insight into the future development of MXene graphitic carbon nitride-based plasmonic ternary photocatalysts.

1. Introduction

The rapid industrialization, increased global warming and depletion of fossil resources have given rise to several environmental and energy-related issues (Ashraf and Hanfiah, 2017; Kumar et al., 2021a). Especially, the pharmaceutical pollutants generated from various industrial plants and hospitals when released directly into the water streams pose threats to humans and aquatic life (Mohan et al., 2020). Hence, it is of utmost importance to treat these pharmaceutical pollutants before releasing into the environment. In this regard, several strategies have been implemented to treat pharmaceutical waste, which involves various chemical and physical methods, such as oxidation, adsorption, reverse osmosis, ion exchange and ultrafiltration (Qin et al., 2015; Wu et al., 2018). Though the use of these processes is limited as most of them simply convert the pollutants from one form to another generating secondary pollutants, which is not desirable. To avoid such issues, photocatalytic processes have arisen as green and sustainable alternatives to eliminate harmful pollutants using renewable sources of energy (solar energy). Photocatalysis, in general, leads to the complete decomposition of organic pollutants without producing any secondary pollutants. Semiconductor-based photocatalysts show high catalytic activity, high turnover number, strong oxidizing ability and several other desirable properties, which make them promising candidates (Chaker et al., 2016; Duoerkun et al., 2020; Sun et al., 2020).

Recently, graphitic carbon nitride (GCN) has gained tremendous attention as a visible light active catalyst for the decomposition of organic pollutants due to its moderate bandgap (~2.7 eV) and high thermal and chemical stability (Cao et al., 2015; Choudhary et al., 2021b; Mishra and Parida, 2021). Despite these excellent properties, GCN exhibits fast recombination of charge carriers and low absorption of visible light, which limits its photocatalytic activity (Dong et al., 2015; Xiang et al., 2019). To improve the photocatalytic efficiency of GCN, numerous strategies have been implemented, such as doping with metals/non-metals and composite formation with other materials, etc. (Bahuguna et al., 2018; Hasija et al., 2019). One such way of utilizing noble metals along with GCN can remarkably enhance its photocatalytic performance due to the plasmonic effect of the noble metals (Kumar et al., 2021b). The surface plasmon resonance (SPR) effect arises from the collective oscillation of surface electrons upon interaction with incident photons of light. The phenomenon of SPR produces highly energetic plasmonic electrons through non-radiative excitations, which contribute to the enhanced photocatalytic activity (Li and Zhang, 2017). Various metals, such as Ag (Jeong et al., 2018), Au (Cheng et al., 2019), Pd (Khan et al., 2018), Ni (Pawar et al., 2019), Cu (DeSario et al., 2017) etc. show plasmonic behaviour and have been utilized in combination with the semiconductor materials for enhanced photocatalytic performance. Among others, gold nanoparticles (Au NP) are highly praised plasmonic materials due to their wide use in photocatalytic, biomedical, photovoltaic and electronic applications (Leng et al., 2018). The use of plasmonic Au NP along with GCN can remarkably enhance its light absorption capability due to the plasmonic effect and prevent the fast recombination of charge carriers due to the creation of the Schottky junction at the Au/GCN interface (Song et al., 2019).

In addition to the use of noble metals, the formation of two-dimensional (2D) heterostructures can also result in enhanced photocatalytic activity by facilitating fast charge transfer at the interface, thus preventing the charge carrier's recombination (Lin et al., 2018; Tang et al., 2019). MXenes are newly discovered anisotropic 2D materials having a structural formula of $M_{n+1}X_nT_x$ (n = 1–3), where M corresponds to the early transition metal, X represents C or N, and T_x presents surface termination groups which can be –O, –F and –OH (Anasori et al., 2017; Wojciechowski et al., 2019). MXenes have a layered structure, tunable elemental composition, large surface area and good structural stability that makes them a potential candidate for photocatalytic applications (Zhu et al., 2017; Ding et al., 2019; Nguyen et al., 2020). The surface termination groups provide hydrophilicity to their surface, which tends to establish strong interactions with other semiconducting materials. The terminal groups can be functionalized or modified accordingly to promote the interactions. In addition, the excellent electrical conductivity assures fast charge carrier transfer (Zhu et al., 2017). MXenes also promote photoinduced charge carrier separation by providing strong support for homogenous dispersion of semiconducting material and simultaneous adsorption of reacting species (Su et al., 2019). The 2D-2D GCN MXene heterojunctions can be formed via electrostatic interactions and van der Waals forces. Due to the difference in the Fermi energy levels of GCN and MXene, close contact between them enhances the separation of photoinduced charge carriers at their interface (Sun et al., 2018). In addition, the Schottky junction at the GCN-MXene interface further assists the photogenerated electron transfer and reduces the fast recombination of charge carriers. Thus, the GCN-MXene heterojunction enhances photocatalytic activity remarkably.

The focus of the manuscript is to rationally design and develop noble metal decorated plasmonic photocatalysts with remarkably improved photocatalytic performance for the elimination of pharmaceutical pollutants from water. A series of novel ternary photocatalysts have been synthesized using plasmonic Au NP, GCN and MXene nanosheets (AGM) via electrostatic assembly. The role of each component is summarized below:

(a) 2D GCN nanosheets are used as the semiconducting photocatalyst, which efficiently harvests energy from visible light.
(b) 2D Ti_3C_2 MXene nanosheets act as excellent electron sink and provide enhanced surface area beneficial for adsorption of pollutants. In addition, due to metallic conductivity and the abundant functional group of MXene, the incorporation of MXene as a cocatalyst in the nanocomposite facilitates the interfacial separation of charge carriers.
(c) Au NP promotes enhanced absorption of visible light through the plasmonic effect and prevents the fast recombination of photogenerated charge carriers.

Therefore, the present study uses above mentioned three components to synthesize a series of AGM nanocomposites by varying the MXene amount in the catalysts as 1, 3, 5 and 10 wt% with respect to AGCN. The prepared AGM nanocomposites were thoroughly characterized before and after treatment and being used for the photocatalytic elimination of cefixime (a colourless pharmaceutical pollutant) from wastewater under visible light. The amount of MXene content was optimized, and a plausible mechanism is proposed with the help of detailed mechanistic investigations. The AGM nanocomposites showed excellent recyclability and can be reused without any significant loss in photocatalytic performance. To the best of our knowledge, this is the first report on a novel ternary plasmonic photocatalyst, Au-GCN-MXene for the degradation of Cefixime pollutant. This work can pave the way for the rational development of efficient and reusable photocatalysts for wastewater treatment using MXene-based materials.

2. Experimental

2.1. Materials synthesis

The procedure adopted for the synthesis of AGM nanocomposites is illustrated pictorially in Scheme 1. The AGM nanocomposites were synthesized via an electrostatic assembly route. In this method, the surface charges of the protonated GCN and Ti_3C_2 MXene were examined. From Zeta potential measurements, it is confirmed that GCN has a positive surface charge ($+18.5$ mV) whereas Ti_3C_2 MXene has a surface negative charge (-13.9 mV). The opposite surface charges can effectively interact with one another to form a few layered GCN/MXene heterostructures. Table 1 summarizes the nomenclature used for the abbreviations and variables used throughout the manuscript.

2.1.1. Synthesis of Au NP

Typically, Au NP has been synthesized by reducing gold precursor, gold (III) chloride trihydrate ($HAuCl_4 \cdot 3H_2O$) via the seed growth method (*Cheng* et al., 2012). In brief, 0.00025 M of $HAuCl_4$ and xxx M trisodium citrate are mixed together in 20 mL of deionized (DI) water. Freshly prepared solution of 0.1 M $NaBH_4$ is added to the above mixture while stirring. The colour of the solution turns pink with the addition of $NaBH_4$ which indicates Au seed particles formation (seed solution). To synthesize the growth solution, 3 g of cetyltrimethylammonium bromide (CTAB) was dissolved in deionized (DI) water. Then, 19.7 μL of 0.00025 M $HAuCl_4$ was added to the CTAB solution, and the solution was heated with continuous stirring until the solution changes its colour to clear orange. Then the solution is allowed to cool down for further use. Subsequently, the required quantities of seed solution, growth solution and ascorbic acid (AA) are mixed to synthesize Au NP of desirable sizes. In short, the growth solution (7.5 mL) was combined with 0.1 M AA solution (0.05 mL) followed by the addition of seed solution (2.5 mL) with constant stirring for about 15 min, and the change in colour of the solution to wine red implying the formation of Au NP of size 5 nm (approximately). Furthermore, to synthesize Au NP with a bigger size (20 nm), the as-prepared solution of Au NP was used as a seed solution. For this 1 mL of the seed solution was mixed with 9 mL of growth solution and 0.1 M AA (0.05 mL) with continuous stirring. Finally, the
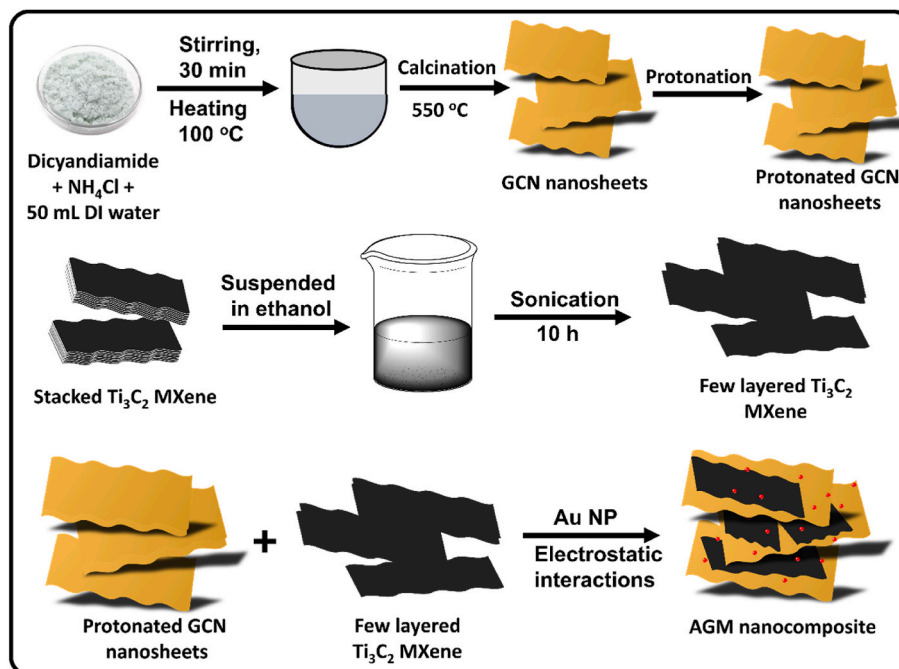
wine-red solution with an approximate size of 20 nm Au NP is obtained. The obtained Au NP were washed multiple times with DI water to remove the surfactant for further use.

2.1.2. Synthesis of GCN nanosheets and protonated GCN nanosheets

The thermal polymerization method using NH_4Cl as a gas template was used for the synthesis of GCN nanosheets (*Alam* et al., 2019; *Choudhary* et al., 2021a). Initially, 2 g dicyandiamide and 10 g of NH_4Cl were mixed in a mortar and pestle. To the resultant mixture, 50 mL of DI water was added, and the mixture was heated at 100 °C overnight to completely evaporate water. The obtained mixture was then crushed into a fine powder and transferred to an alumina crucible. Further, the crucible was heated with programmed heating rates (400 °C with a rate of 5 °C min^{-1}; 500 °C with a rate of 2 °C min^{-1} and 550 °C with a rate of

Table 1
Nomenclature table for the abbreviations used.

Abbreviations	Definition	Abbreviations	Definition
AA	Ascorbic acid	C	Concentration
AGCN	Au NP decorated GCN	CB	Conduction band
AGM01	Au NP GCN/MXene (1 wt% of MXene)	eV	Electron volt
AGM03	Au NP GCN/MXene (3 wt% of MXene)	h$^+$	Holes
AGM05	Au NP GCN/MXene (5 wt% of MXene)	OH$^\bullet$	Hydroxyl radical
AGM10	Au NP GCN/MXene (10 wt % of MXene)	μL	Microliter
CTAB	Cetyltrimethylammonium bromide	mg	Milligram
CFL	Compact fluorescence light	mL	Millilitre
EDX	Energy dispersive x-ray spectroscopy	M	Molar
Au NP	Gold nanoparticles	I-t	Photocurrent time
GCN	Graphitic carbon nitride	k	Rate constant
IPA	Isopropyl alcohol	$O_2^-{}^\bullet$	Superoxide radicals
PEC	Photoelectrochemical	t	Time
PL	Photoluminescence	VB	Valence band
TEA	Triethanolamine	W	Watt

Scheme 1. Pictorial demonstration for the demonstration of Au NP decorated GCN/MXene (AGM) nanosheets.

1 °C min^{-1}) and then heated at 550 °C for 2 h. At elevated temperatures, NH_4Cl releases a gaseous product resulting in intercalated gaseous bubbles, separating the GCN nanosheets. The crucible is allowed to cool down, and the yellow powder obtained was GCN. For the protonation of GCN, 3 g of GCN was ultrasonicated in 100 mL of HCl for 2 h. The reaction mixture was further stirred at room temperature for 4 h. Finally, the product was washed several times with DI water to obtain protonated GCN.

2.1.3. Preparation of Au-GCN nanocomposite

The preparation of Au-GCN (AGCN) nanocomposite was done by using an electrostatic self-assembly route. For this, 100 mg of protonated GCN and 500 μL of as-synthesized Au NP were dispersed through sonication in 20 mL of DI water for 1 h. The resultant mixture was then stirred for 3 h at room temperature.

2.1.4. Preparation of Au-GCN-MXene (AGM) nanocomposites

The AGM nanocomposites were prepared via an electrostatic self-assembly route (*Xu* et al., *2021*). Initially, Ti_3C_2 MXene was sonicated in ethanol for 10 h. The few-layered Ti_3C_2 MXene was further centrifuged and dried in the oven overnight for further use. To prepare the desired nanocomposites, 1 wt%, 3 wt%, 5 wt% and 10 wt% of Ti_3C_2 MXene were added to 100 mg of AGCN in 20 mL of DI water and further sonicated for half an hour and kept stirred for 3 h. The obtained final product was washed with DI water several times and dried in the oven overnight. These nanocomposites were labelled as AGM01, AGM03, AGM05 and AGM10, respectively. The real-time photographs of the nanocomposites are shown in Fig. S1 (Supplementary data).

2.2. Photocatalytic pollutant degradation

The photocatalytic performance of the as-synthesized nanocomposites was investigated for the degradation of a colourless pharmaceutical pollutant, cefixime. For the photocatalytic degradation of cefixime (Kumar et al., 2018a) a previously reported procedure was implemented. Typically, the as-synthesized photocatalyst (20 mg) was suspended in a 50 mL aqueous solution of cefixime having a concentration of 5×10^{-5} M. The prepared dispersion was subjected to visible light irradiation using two 45 W compact fluorescence light (CFL) lamps.

Furthermore, 1 mL of aliquot solution was collected from the reaction mixture after an interval of 15 min. The UV–visible spectroscopic method was used to monitor the reaction progress.

2.3. Photoelectrochemical studies

The photoelectrochemical measurements were conducted using a three-electrode photoelectrochemical (PEC) cell (Metrohm, Autolab). To prepare the working electrode 4 mg of the photocatalyst was dispersed in a mixture of Nafion (20 μL) and ethanol (500 μL). Furthermore, the samples were evenly spread on an indium tin oxide rigid glass substrate. A reference electrode (Ag/AgCl) and a counter electrode (Pt wire) were used for the experiment. All three working, counter and reference electrodes were dipped into 0.1 M Na_2SO_4 electrolytic solution for PEC measurements. A 45 W compact fluorescent lamp (CFL) emitting visible light was used as a source for visible light. The PEC investigations of the prepared photocatalysts were done under dark and light conditions.

3. Results and discussion

3.1. Structural studies

The x-ray diffraction (XRD) analysis was done to examine the crystal structure and the purity of the nanocomposites (Fig. 1a). GCN exhibits two characteristic diffraction peaks at 13.0° and 27.5°, corresponding to the (100) and (002) reflection planes. The diffraction peak at 27.5° is associated with interplanar stacking of aromatic systems, and the peak at 13.0° arises due to in-plane tritriazine units. The XRD patterns of the AGM nanocomposites predominantly exhibit the diffraction peaks belonging to GCN, which is the main component of the nanocomposites. In addition, the prepared nanocomposites also exhibited additional diffraction peaks at 38.2° and 44.4°, which corresponds to (111) and (200) planes of Au NP confirming their presence (Chen et al., 2014; Geng et al., 2017). For Ti_3C_2 MXene, all the diffraction peaks obtained match well with the reported literature (Debow et al., 2021). The diffraction peaks at (002) and (004) shift to lower degrees together, which indicates that the Ti–Al bond was interrupted. No new XRD peak is observed in AGM nanocomposites which suggest that GCN and Ti_3C_2
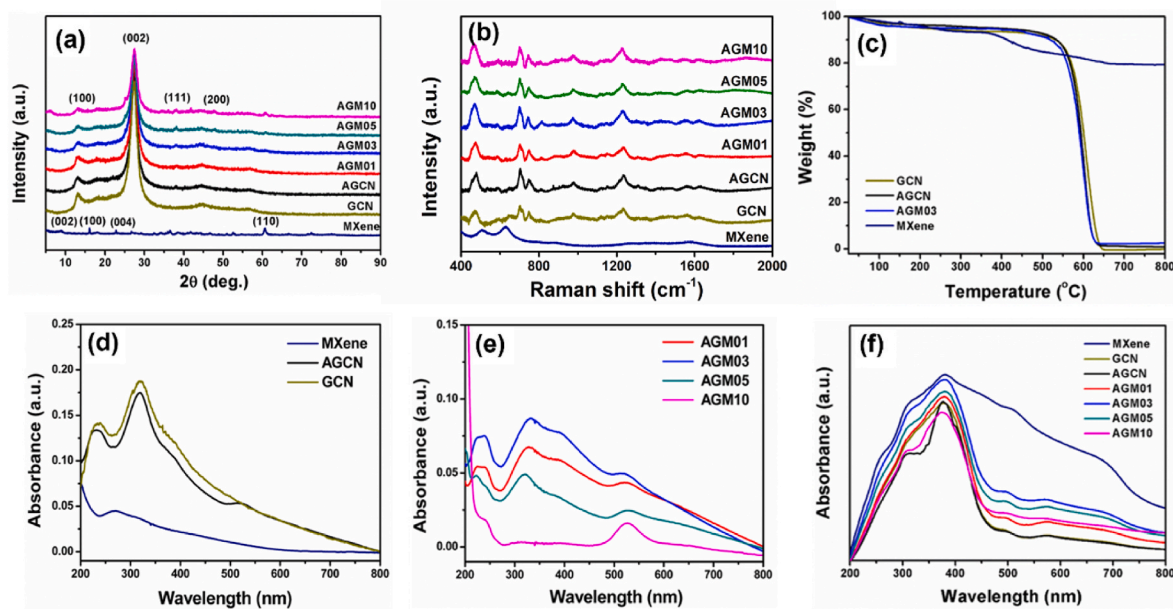

Fig. 1. (a) XRD patterns and (b) Raman spectra of GCN, AGCN, Ti_3C_2 MXene and AGM nanocomposites, (c) TGA plots of GCN, AGCN, Ti_3C_2 MXene and representative AGM03 nanocomposite, UV–visible spectra of (d) GCN, AGCN and MXene, (e) AGM nanocomposites and (f) solid-state DRS of GCN, AGCN, MXene and AGM nanocomposites.

are combined via electrostatic interactions (Peng et al., 2018; Sun et al., 2018).

Fig. 1b depicts the Raman spectra for GCN, AGCN, MXene and the prepared AGM catalysts. The spectra for GCN show three significant peaks at 1560, 1233 and 708 cm^{-1}. The peak centred at 1560 cm^{-1} arises due to the stretching modes of the C=N whereas the peak at around 708 cm^{-1} belongs to the breathing modes of the s-triazine ring. The peak at 1233 cm^{-1} represents the imperfections or defects in the graphite structure (Zinin et al., 2009; Pawar et al., 2015). For AGCN, the peak intensity at 708 cm^{-1} is a bit enhanced due to the presence of Au NP. The enhancement can be the plasmonic effect of the Au NP. Although the amount of Au NP and Ti_3C_2 MXene used is very small but still the enhancement in the intensity of Raman peaks can be observed in AGM nanocomposites (Zhao et al., 2016; Rajender et al., 2017).

The thermal stability of the prepared catalysts was examined by thermogravimetric analysis (TGA) and the obtained plots are shown in Fig. 1c. It is observed that GCN shows excellent thermal stability up to 540 °C as its initial weight loss percent is very low. The evaporation of the water molecules adsorbed on the surface of the catalyst causes initial weight loss. After 550 °C GCN starts decomposing, and by 650 °C, complete disintegration of the GCN network was observed. Whereas AGCN seems to be slightly more stable than GCN due to the presence of Au NP. Further, the ternary nanocomposite, AGM03 shows better stability than GCN and AGCN catalysts due to the presence of Ti_3C_2 MXene. As observed from the TGA plots, Ti_3C_2 MXene is quite stable up to 800 °C. Since the weight percent of Ti_3C_2 MXene is significantly less in the as-prepared nanocomposites, hence they are not as stable as Ti_3C_2 MXene (González-Mendoza and Cabrera-Lara, 2015).

The UV–visible spectra of the as-prepared photocatalysts was measured and is presented in Fig. 1d and e. GCN shows an intrinsic absorption edge at around 470 nm, but in AGCN, a peak centred at 520 nm was also observed that belongs to the plasmonic band of Au NP

(Abdelhalim et al., 2012; Cheng et al., 2013). No sharp absorption edge is observed for Ti_3C_2 MXene as it is a metallic and full-spectrum absorber (Xu et al., 2021). Generally, the involvement of Ti_3C_2 MXene does not result in an appreciable redshift in UV–vis spectra (Ran et al., 2017). In the ternary AGM nanocomposites, the presence of a peak around 520 nm corresponds to the Au NP in the nanocomposites. The capacity to absorb radiation is reduced as the content of Ti_3C_2 MXene is increased. This can be ascribed to the dark black colour of Ti_3C_2 MXene, which hinders the light absorption capability of the photocatalyst. The as-synthesized photocatalysts were further analyzed by UV–visible diffuse reflectance spectroscopy (DRS) for the examination of optical properties. The absorption band of the AGM is concentrated at around 375 nm, as GCN is the main component in the catalysts. It was observed from Fig. 1e that the addition of Au NP and Ti_3C_2 MXene has resulted in the greater absorption of visible region. The absorption bands of the AGM photocatalyst covers the whole visible region which suggests that the as-prepared catalysts are highly photoactive in nature (Yin et al., 2020; Ahmed et al., 2021; Kumar et al., 2021b).

3.2. Morphological and compositional studies

The morphology and structure of the nanocomposites prepared were verified by using the scanning electron microscopic (SEM) technique. Fig. 2a, b shows the SEM image for GCN, which indicates that GCN has a lamellar structure consisting of an irregular thin sheet (Tan et al., 2015). Small-sized Au NP were found to be deposited on the surface of GCN Fig. 2c and d resulting in the formation of AGCN nanocomposite. Fig. 2e–f shows the typical morphology of the Ti_3C_2 MXene. Un-delaminated Ti_3C_2 MXenes were found to be of stacked morphology with multi-layered structure (Fig. 2e) (Cao et al., 2017; Feng et al., 2019), but on sonication, the Ti_3C_2 MXene structure is swelled in such that it converts into a flake-like structure which is indicative of the fact

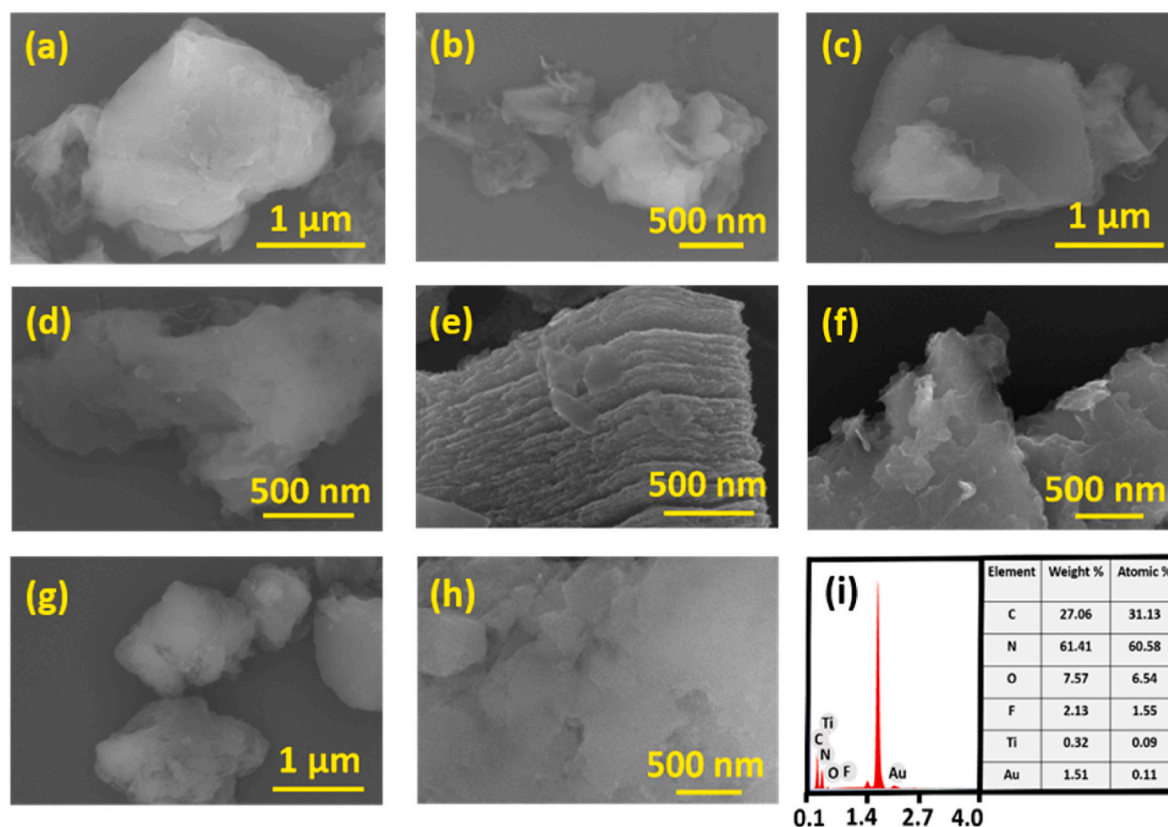| Element	Weight %	Atomic %
C	27.06	31.13
N	61.41	60.58
O	7.57	6.54
F	2.13	1.55
Ti	0.32	0.09
Au	1.51	0.11

Fig. 2. SEM images of (a, b) GCN, (c, d) AGCN, (e, f) Ti_3C_2 MXene, (g h) AGM03 and (i) EDX spectrum of AGM03 photocatalyst. Insert of (i) represents the weight and atomic percentage of the elements presented in the representative AGM03 nanocomposite.

that the delamination process has been achieved as shown in Fig. 2f (Feng et al., 2019). The morphology of the prepared ternary nanocomposites, AGM03, was also observed, predominantly showing 2D nanosheets (Fig. 2g and h). The existence of all the elements in the AGM03 photocatalyst was further confirmed by energy dispersive x-ray spectroscopy (EDX). Finally, the weight and atomic percentage of the elements in the representative photocatalyst, AGM03 are shown in Fig. 2i (insert).

The nanoscale morphologies of the as-synthesized catalysts were investigated through transmission electron microscopy (TEM). Fig. 3a–c shows the TEM images of GCN at different scales, which depicts crumbled sheet-like morphology. TEM images of Ti_3C_2 MXene show compact sheet-like morphology formed due to the stacking of thin layered nanosheets (Fig. 3d–f). Fig. 3g–i represents the TEM images of the AGM03 catalyst, which shows the 2D nanosheets-like morphology, wherein the GCN and Ti_3C_2 MXene nanosheets are stacked upon one another. The AGM03 nanocomposite shows uniform distribution of Au NP over the 2D-2D heterostructure. Fig. 3j shows the EDX spectra of AGM03 nanocomposite, which reveals the existence of constituent

elements. Fig. 3k-p presents the elemental mapping images of AGM03 nanocomposite that confirm the presence and homogeneous distribution of all the elements.

The chemical composition and interactions between GCN, Au NP and Ti_3C_2 MXene were analyzed using XPS analysis. The survey spectra (Fig. S2, supplementary data) show the existence of C, N and O in GCN structure. The survey spectra of Ti_3C_2 MXene, binding energy peaks at 285.1, 455.5, 531.9 and 685.1 eV corresponding to C 1s, Ti 2p, O 1s and F 1s, respectively, wherein the F-species arises from the functionality and O species from surface oxygen/hydroxyl groups. The survey spectrum of AGM03 nanocomposite confirmed the presence of C, N, Ti, O and Au in the as-prepared material. Specifically, peaks at 399.2, 288.1, 532.1, 458.6 eV and 83.2 are attributed to N 1s, C 1s, O 1s, Ti 2p and Au 4f. High-resolution XPS spectra in the C-1s region of the Ti_3C_2 MXene revealed three main peaks occurring at 284.8, 286.5 and 288.2 eV, which may originate from Ti–C, C–C and C–O interactions, respectively (Fig. 4a). The main peak at 288.2 eV in the C-1s XPS spectra in AGM03 indicates the existence of the $N=C-N_2$ coordination (Wen et al., 2017). The N 1s can be fitted into two peaks at 398.7 eV and 400.5 eV, which
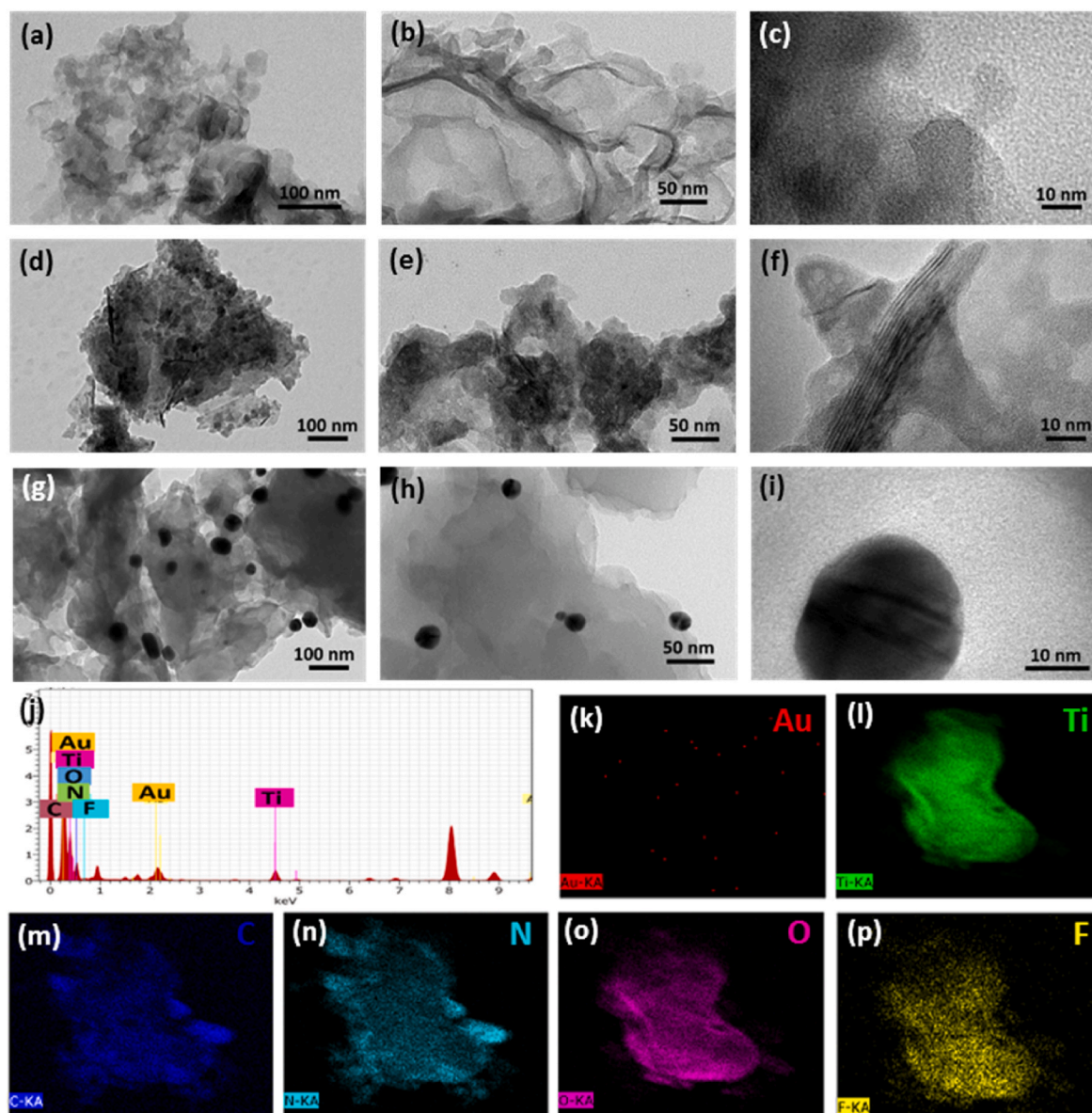

Fig. 3. TEM images of (a–c) GCN, (d–f) Ti_3C_2 MXene, (g–i) AGM03 nanocomposite and (j) EDX spectra of AGM03 nanocomposite, (k–p) elemental mapping of representative AGM03 nanocomposite.
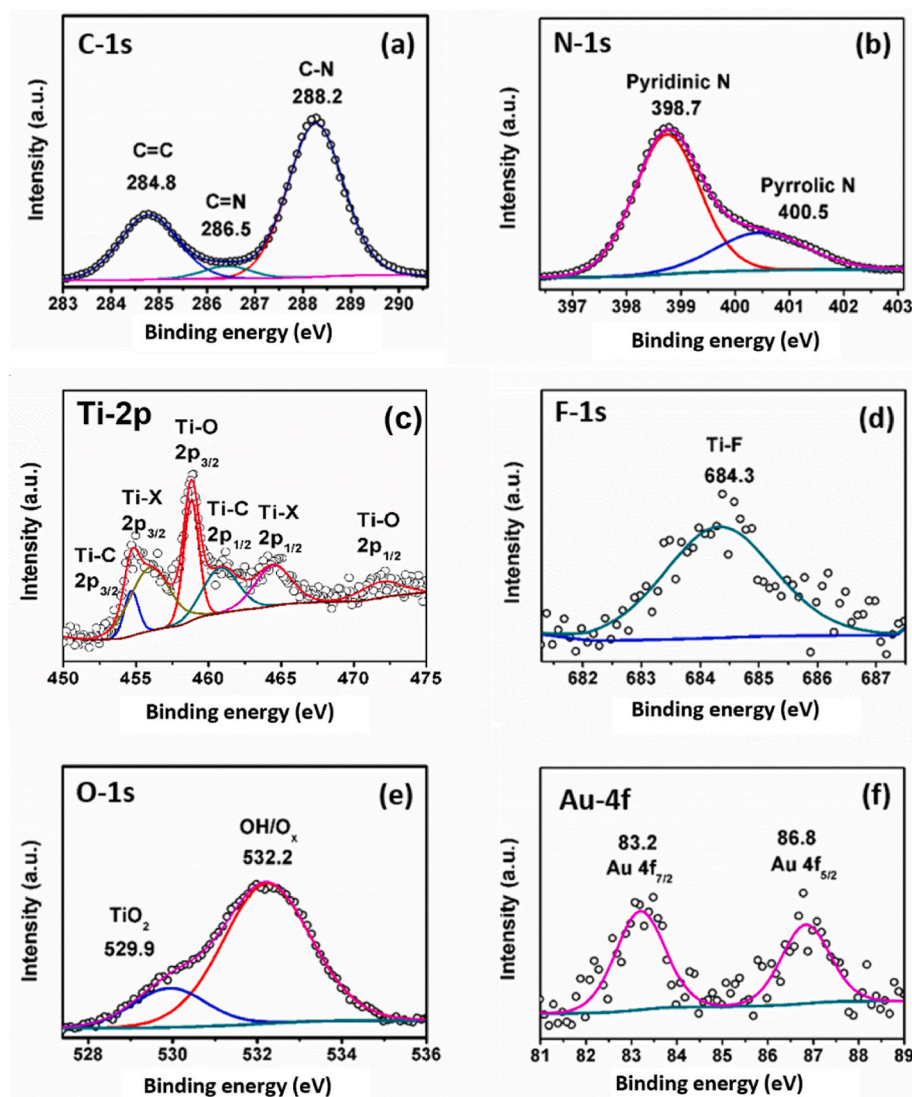
Fig. 4. X-ray photoelectron spectra of (a) C 1s, (b) N 1s, (c) Ti 2p, (d) F 1s, (e) O 1s and (f) Au 4f of AGM03 nanocomposite.

indicates the presence of pyridinic-N and pyrrolic-N atoms (Fig. 4b) (Tan et al., 2015; Wen et al., 2017). Furthermore, the Ti-2p peak can be deconvoluted into multiple peaks indicating the presence of Ti–C, Ti–X and Ti–O bonds (Fig. 4c). The single peak at 684.3 eV corresponds to the Ti–F bond in the nanocomposite arising from the F functionality in the Ti_3C_2 MXene (Fig. 4d). The peaks for O 1s at 529.9 and 532.2 eV can be assigned to Ti–O and C–Ti-O_x or C–Ti-$(OH)_x$, respectively, as shown in Fig. 4e (Halim et al., 2016; Cao et al., 2017; Shah et al., 2017). The Au 4f spectra are deconvoluted into two different peaks at 83.2 and 86.8 eV that can be attributed to Au $4f_{7/2}$ and Au $4f_{5/2}$, respectively, confirming the metallic state of Au NP as shown in Fig. 4f (Tunc et al., 2005).

Brunauer-Emmett-Teller surface area (S_{BET}) technique was used to determine the surface properties of the photocatalysts, and the obtained results are summarized in Table S1 (supplementary information). It was observed that the surface area of AGCN catalyst was found to be higher than that of GCN due to the incorporation of small size Au NP. The AGM03 nanocomposite exhibits the highest surface area due to the incorporation of Au NP and Ti_3C_2 MXene nanosheets. The higher surface area of nanocomposites, is quite favourable for the high adsorption of the pollutants, thereby resulting in enhanced photocatalytic activity. The incorporation of Ti_3C_2 MXene nanosheets leads to more numbers of surface active sites in AGCN, thus enhancing the tendency of pollutant adsorption (Zhang et al., 2010).

3.3. Photocatalytic pollutant degradation studies

The photocatalytic potential of the catalysts was investigated for the mineralization of a colourless pharmaceutical pollutant, cefixime (the chemical structure is shown in Fig. S3, supplementary data) was performed under visible light irradiation. The progress of the decomposition process was monitored using UV–visible spectroscopy. A constant decrease in the absorbance peak of cefixime (centred at 286 nm) was found with respect to time. The time-dependent UV–visible spectra for the decomposition of cefixime are shown in Fig. S4 (supplementary data). To calculate the degradation percentage the following eq. (1) was used (Zhu et al., 2016):

$$\% \text{ degradation} = \frac{C_o - C_t}{C_o} \times 100 \qquad (1)$$

Here, C_0 is the concentration of the pollutant at time 0 min and C_t is the pollutant concentration after time t min.

The histograms depicted in Fig. 5 represent the decomposition of cefixime under visible light using different photocatalysts. Also, two control experiments, one without catalyst (WC) and another under dark conditions were performed to ensure the photocatalytic potential of as-prepared catalysts. The percentage degradation of cefixime observed WC, under dark conditions, with GCN, AGCN, AGM01, AGM03, AGM05
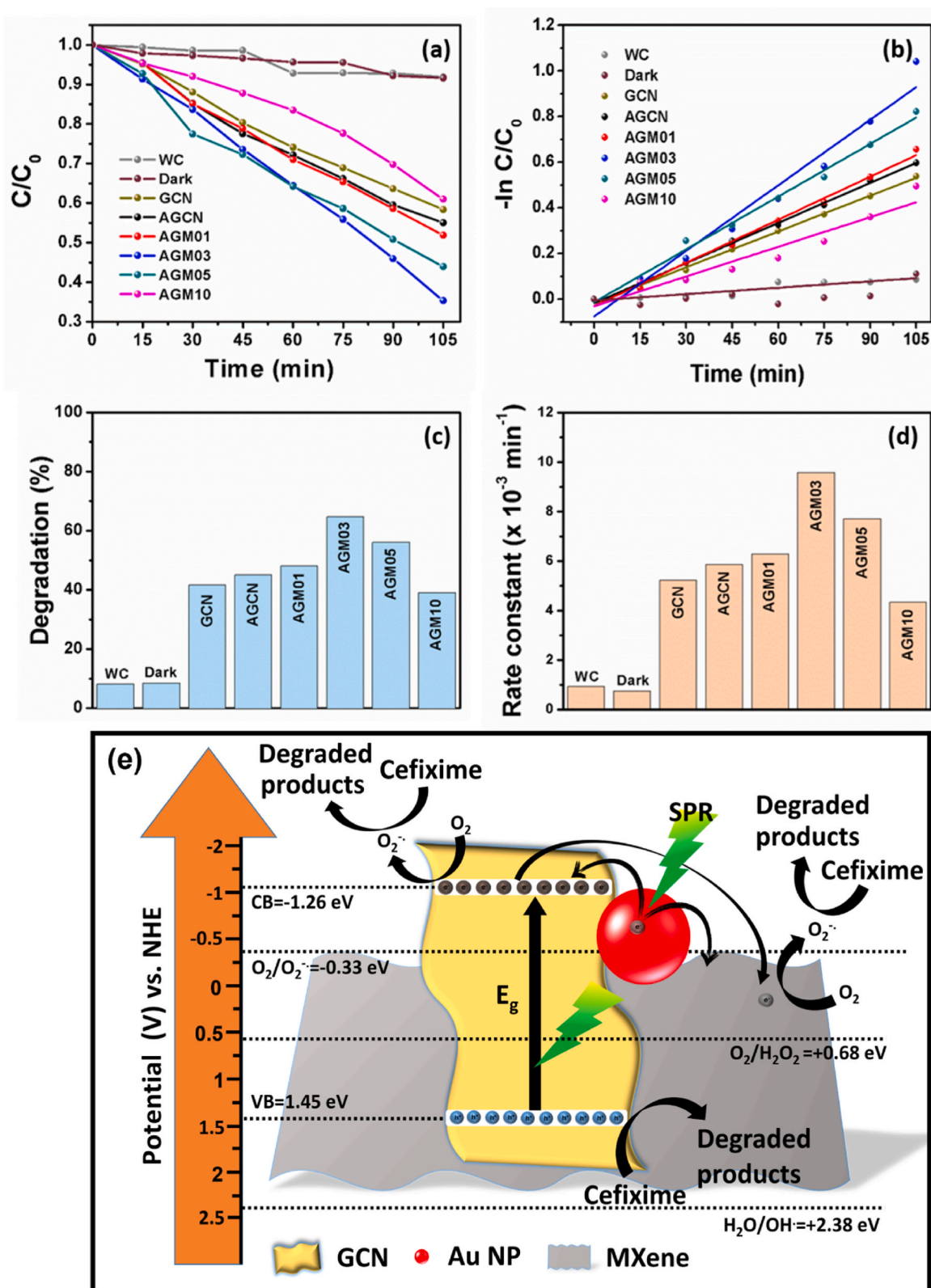
Fig. 5. (a, b) Kinetic curve of cefixime decomposition, (c) histogram presenting the degradation rate (%) of cefixime and (d) rate constants for all the catalysts under visible light, (e) schematic illustration of photocatalytic decomposition mechanism of cefixime using AGM nanocomposites under visible light illumination.

and AGM10 under visible light irradiation was shown in Fig. 5a, c. In the absence of photocatalysts, very low (9.00%) degradation of cefixime was found when illuminated with visible light. Under dark conditions, the degradation was just 8.30% which confirms the role of visible light

in the degradation process. GCN shows approximately 41.63% of cefixime degradation in 105 min under visible light irradiations. The small-sized Au NP decorated over GCN (AGCN photocatalyst) increases the photocatalytic activity to 44.99% due to their plasmonic effect.
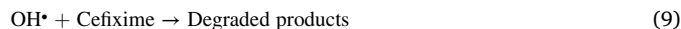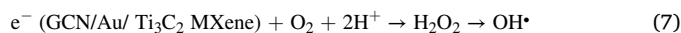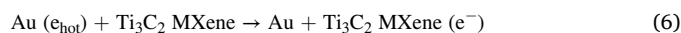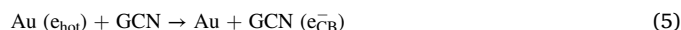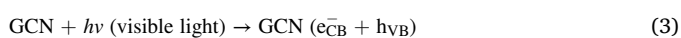
Among all the AGM nanocomposites, the highest catalytic activity (64.69%) is shown by the AGM03 nanocomposite which can be ascribed to the combined effect of plasmonic Au NP and Ti_3C_2 MXene due to which the rate of generation of active species is enhanced, whereas the charge recombination rate is reduced to an appreciable extent. Furthermore, for AGM05 and AGM10 nanocomposites, the photocatalytic activity is decreased to a certain extent which can be attributed to the higher content of MXene, which gets deposited over the surface of GCN nanosheets and does not allow visible light to pass through to reach active sites of GCN. As a result, there is a limited generation of photoinduced charge carriers, which further decreases the number of active species, thereby decreasing the degradation rate. Besides, the kinetics of the degradation was fitted with the model reactions, as shown in Fig. 5b. It was observed that the degradation of cefixime follows the pseudo first-order model as mentioned in eq. (2).

$$-\ln\left(C_t / C_0\right) = kt \tag{2}$$

Here, k is the rate constant for the degradation process.

Furthermore, based on the acquired results, a plausible photocatalytic mechanism has been formulated which is depicted in Fig. 5e. In brief, on illuminating visible light, the electrons get excited from the valence band (VB) to the conduction band (CB) in GCN, thereby generating electron-hole pairs. Since the Fermi energy level of the n-type semiconductor, GCN, is at a higher negative potential value than the Fermi energy level of Ti_3C_2 MXene, the photoinduced electrons will move from GCN CB to the surface of highly conducting Ti_3C_2 MXene (Ding et al., 2019). GCN and Ti_3C_2 MXene components, when used individually as catalysts, suffer from many limitations, the major being the fast recombination rate of electron-hole pairs which results in decreased photocatalytic activity. However, if used combinedly with GCN and Ti_3C_2 MXene, the electrons from GCN are transferred to Ti_3C_2 MXene, where a fixed positive charge is developed near the GCN and Ti_3C_2 MXene heterojunction, resulting in the formation of the Schottky barrier which aids in ruling out this major limitation of recombination to some extent (Yin et al., 2020). Also, the free electrons in Au NP move to higher energy levels due to the SPR effect, which further transfers from to the CB of GCN or to Ti_3C_2 MXene nanosheets. Now, these electrons will react with adsorbed water molecules to form active radical species, superoxide anion ($O_2^-\bullet$) and hydroxyl radical ($OH^\bullet$) species, responsible for the degradation of cefixime (Wojciechowski et al., 2019; Biswal et al., 2021). Hence, it can be concluded that the electron transfer involves two pathways. One is via the Schottky junction, which effectively captures the existing electrons and acts as an electron trap. Secondly, the strong plasmonic effect of Au NP, leads to the fast transport of electrons in the composite photocatalyst (Kumar et al., 2021b). The proposed mechanism is in good agreement with earlier reported literature (Mostafaloo et al., 2019; Salimi et al., 2019; Zhang et al., 2021). On illuminating visible light, electrons will excite to the CB of GCN, leaving the electrons in the VB (eq. (3)). The Au NP shows the SPR effect when illuminated with visible light resulting in the production of highly energetic hot electrons. However, in the nanocomposite Au NP plays a dual role, as an electron acceptor due to its lower Fermi energy level than CB of GCN and as a photosensitizer to capture light photons due to the SPR effect (eqs. (4) and (5)) (Clavero, 2014). In addition to this. Au NP can also transfer its electrons to Ti_3C_2 MXene as the Fermi energy level of this material is lower than the Fermi energy level of Au NP (eq. (6)). Furthermore, electrons in Au NP and Ti_3C_2 MXene, and separated electron-hole pairs in GCN, will react with the adsorbed water molecules resulting in the formation of hydrogen peroxide and finally $OH^\bullet$ (eqs. (7) and (8)) (Biswal et al., 2021a; Chen et al., 2021). Ultimately, these $OH^\bullet$ reacts with the pollutant molecule, cefixime to give the fragmented products (eq. (9)). The degradation of cefixime using AGM nanocomposites under visible light irradiation can be depicted by the following equations:

$$GCN + h\nu \text{ (visible light)} \rightarrow GCN \left(e_{CB}^- + h_{VB}^+\right) \tag{3}$$

$$Au\ NP + \text{visible light} \rightarrow Au\ (e_{hot}) \tag{4}$$

$$Au\ (e_{hot}) + GCN \rightarrow Au + GCN\ (e_{CB}^-) \tag{5}$$

$$Au\ (e_{hot}) + Ti_3C_2\ MXene \rightarrow Au + Ti_3C_2\ MXene\ (e^-) \tag{6}$$

$$e^-\ (GCN/Au/\ Ti_3C_2\ MXene) + O_2 + 2H^+ \rightarrow H_2O_2 \rightarrow OH^\bullet \tag{7}$$

$$h_{VB}^+\ (GCN/Au) + H_2O \rightarrow OH^\bullet \tag{8}$$

$$OH^\bullet + Cefixime \rightarrow \text{Degraded products} \tag{9}$$

Furthermore, to support the photocatalytic mechanism of the nanocomposite active species trapping experiments were performed under visible light irradiations (Fig. 6a). For the mineralization of the pollutant, the active species such as superoxide radicals ($O_2^-\bullet$), hydroxyl radicals ($OH^\bullet$) and holes (h^+) are playing the important role. The triethanolamine (TEA), isopropyl alcohol (IPA) and chloroform was used as a radical active scavenger for h^+, $OH^\bullet$ and $O_2^-\bullet$, respectively. The hydroxyl radical scavenger IPA gives almost no suppression effect on the removal of cefixime from the system indicating the minor role of the hydroxyl radicals in the degradation process. Consequently, the $O_2^-\bullet$ radical scavenger shows a slight suppression effect, indicating the comparatively higher contribution of $O_2^-\bullet$ radicals in the process. In the presence of TEA, the remarkable decrease in the photocatalytic performance of the catalyst revealing h^+ acts as major active radical for the degradation of cefixime under visible light irradiations. The photocatalytic performance of the as compared photocatalyst was compared with the previously reported GCN-based photocatalysts as shown in Table S2 (supplementary data). The table illustrates the comparison of irradiation source, pollutant concentration, catalyst amount and degradation efficiency of different pollutants.

3.4. Photoluminescence and photoelectrochemical investigations

Photoluminescence (PL) investigations were used to study the influence of the photogenerated charge carriers on the photocatalytic activity and the obtained results are presented in Fig. 6a. To record the PL spectra of the nanocomposites, 360 nm was used as the excitation wavelength. Upon illumination of the samples under visible light irradiations, electrons get excited to higher energy levels. When these excited electrons come back to lower energy levels, the emitted energy can be recorded in the form of photoluminescence. The faster the recombination of the charge carriers, lower the photocatalytic performance. Fig. 6b shows that the highest emission peak at 440 nm can be ascribed to the charge carrier recombination band transitions. The lowest intensity of the AGM03 nanocomposite indicates the slow recombination rate of the charge carriers, thereby expected to show the best photocatalytic performance. Furthermore, it was found that the increase in the GCN content results in an agglomeration that starts acting as recombination centres for the photoinduced charge carriers (Kumar et al., 2018b).

Further, to confirm the effective separation of the charge carriers (electrons and holes), photoelectrochemical (PEC) investigations were performed. Fig. 6c shows the photocurrent time (I–t) curves of GCN, AGCN and AGM03 nanocomposite under visible light irradiations. In the absence of the light photons, the photocurrent decays to zero suggesting the recombination of charge carriers. On illuminating visible light, the observable photocurrent density in GCN is because of the effective separation of photogenerated charge carriers. The addition of Au NP enhances the photocurrent density of the nanocomposite which can be ascribed to the formation of the Schottky junction between Au NP and GCN that promotes charge carrier separation at interfaces. In addition to this Au NP also acts as a plasmonic photosensitizer under visible light. The highest photocurrent density of the AGM03 nanocomposite ($\sim$5 μA cm^{-2}) can be ascribed to the synergistic effect of the presence of Au NP and $Ti_3C_2T_x$ MXene nanosheets. MXene nanosheets are excellent
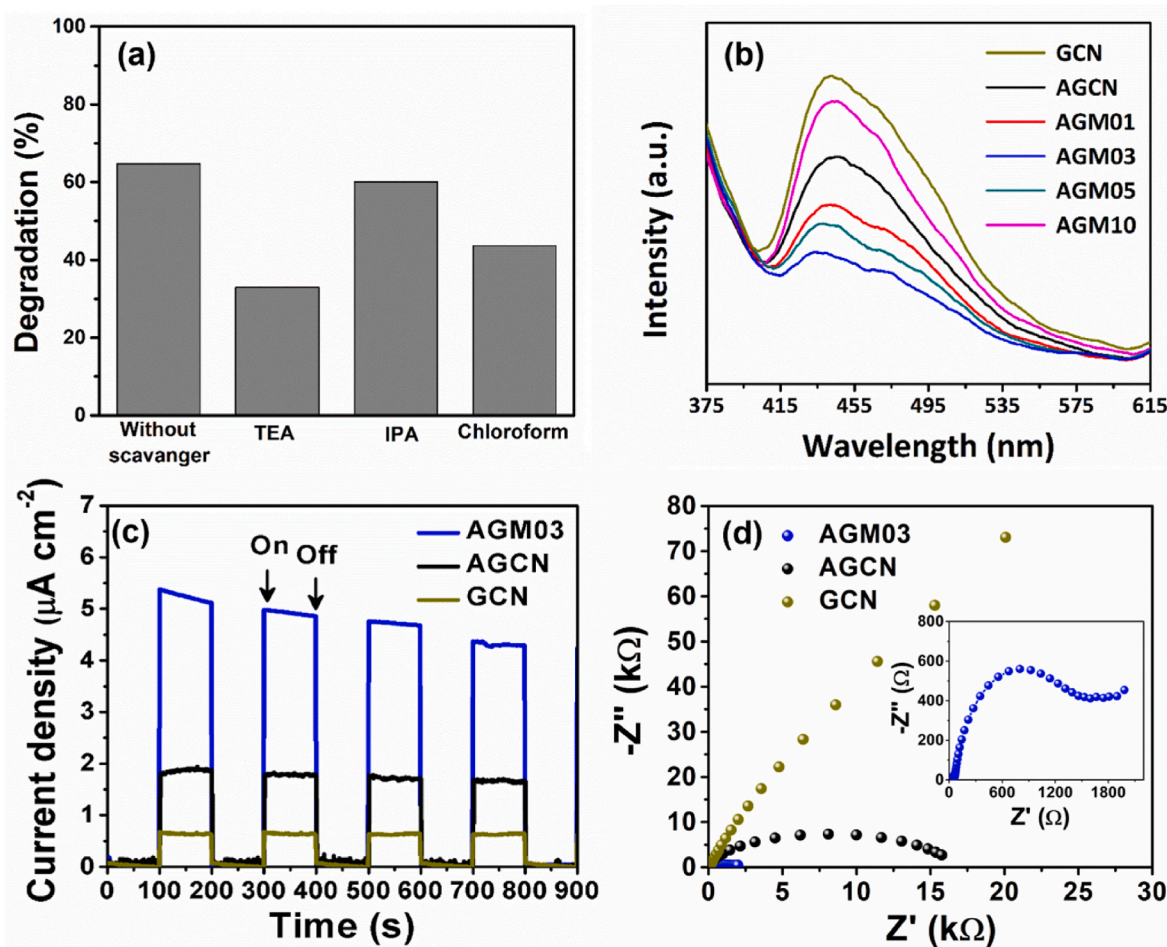
Fig. 6. (a) Active species trapping experiments of AGM nanocomposite using TEA, IPA and chloroform under visible light irradiations. (b) Photoluminescence spectra of AGM nanocomposites, (c) transient photocurrent responses and (d) Nyquist plots of GCN, AGCN and AGM03 nanocomposite.

acceptors and transporter of electrons due to their conducting nature. This justifies the role of the Au NP and MXene nanosheets in improving the lifetime of the photogenerated charge carriers to enhance the photocatalytic performance of the AGM.

Electrochemical impedance spectroscopy (EIS) studies of control samples and as-prepared nanocomposites were examined under visible light illumination. The obtained Nyquist plots are shown in Fig. 6d. The diameter of the semicircle signifies the resistance of charge transfer at photocatalyst/electrolyte interfaces. For instance, the AGM03 composite samples showed a small diameter of the semicircle compared with other samples. This indicates that the presence of the Au NP and MXene nanosheets drastically enhances the charge transfer across the interface.

In practical application, the sustainable performance of photocatalyst after each cycle of the water treatment process is crucial. Therefore, the recyclability of the benchmarking nanocomposite, AGM03 up to three cycles was tested for the degradation of cefixime. The nanocomposite was recovered and washed several times after the completion of every cycle. Only a minor decrease in the photocatalytic activity was observed even after the completion of three cycles, indicating the reusability of the photocatalyst (Fig. S5a, supplementary data). The structural integrity of the recovered photocatalyst was analyzed using XRD and SEM techniques after three cycles as shown in Fig. S5b and Fig. S5c (supplementary data), respectively. It is observed that even after 3 cycles, the AGM03 photocatalyst was highly stable and structurally intact.

4. Conclusions

In summary, it was successfully demonstrated that the simultaneous loading of plasmonic Au NP and Ti_3C_2 MXene as co-catalysts can effectively boost the photocatalytic performance of GCN for the removal of a colourless pharmaceutical pollutant. Herein, a novel plasmonic photocatalyst consisting of Au NP, GCN and Ti_3C_2 MXene nanosheets has been designed using an electrostatic assembly route. The optimized photocatalyst having 3 wt% Ti_3C_2 MXene exhibits remarkably enhanced photocatalytic performance due to the mutual effect of different materials used, which facilitates excellent charge carrier separation and an increased number of active sites. Impressively, the heterojunction formed due to dual cocatalysts (Au NP and Ti_3C_2 MXene) onto the semiconducting material GCN provides distinguished features of excellent charge separation and transport, abundant reaction sites, efficient harvesting of visible light, thereby exhibiting the 64.7% removal of the cefixime in 105 min which is much higher than bare GCN. On increasing Ti_3C_2 MXene content beyond 3 wt%, a decrease in the photocatalytic performance was found, due to the hindrance to the light photon absorption because of an excessive amount of Ti_3C_2 MXene. This work unlocks new opportunities for the development of highly efficient MXene-based multi-component plasmonic photocatalysts for eliminating harmful water pollutants.

Author contributions

Ajay Kumar - Conceptualization; Formal analysis; Methodology; Data curation; Writing – original draft. **Palak Majithia** - Methodology;

Data curation; Formal analysis. **Priyanka Choudhary** - Conceptualization; Data curation; Formal analysis; Writing – review & editing. **Ian Mabbett** - Data curation; Formal analysis; Writing – review & editing. **Moritz F. Kuehnel** - Data curation; Formal analysis; Funding acquisition; Writing – review & editing. **Sudhagar Pitchaimuthu** - Supervision; Validation; Funding acquisition; Formal analysis; Writing – review & editing. **Venkata Krishnan**- Conceptualization; Project administration; Supervision; Validation; Funding acquisition; Formal analysis; Writing – review & editing.

Declaration of competing interest

The authors declare that they have no known competing financial interests or personal relationships that could have appeared to influence the work reported in this paper.

Data availability

Data will be made available on request.

Acknowledgments

Appendix A. Supplementary data

Supplementary data to this article can be found online at https://doi.org/10.1016/j.chemosphere.2022.136297.

References

Abdelhalim, M.A.K., Mady, M.M., Ghannam, M.M., 2012. Physical properties of different gold nanoparticles: ultraviolet-visible and fluorescence measurements. J. Nanomed Nanotechol 3, 178–194.

Ahmed, A., Hayat, A., Nawaz, M.H., Chaudhry, A.A., John, P., Nasir, M., 2021. Fluorescence quenching mediated detection of hydrogen peroxide using tungsten incorporated graphitic carbon nitride nanoflakes. RSC Adv. 11, 7479–7491.

Alam, K.M., Kumar, P., Kar, P., Thakur, U.K., Zeng, S., Cui, K., Shankar, K., 2019. Enhanced charge separation in gC$_3$N$_4$–BiOI heterostructures for visible light driven photoelectrochemical water splitting. Nanoscale Adv. 1, 1460–1471.

Anasori, B., Lukatskaya, M.R., Gogotsi, Y., 2017. 2D metal carbides and nitrides (MXenes) for energy storage. Nat. Rev. Mater. 2, 1–17.

Ashraf, M.A., Hanfiah, M.M., 2017. Recent advances in assessment on clear water, soil and air. Environ. Sci. Pollut. Res. 24, 22753–22754.

Bahuguna, A., Choudhary, P., Chhabra, T., Krishnan, V., 2018. Ammonia-Doped polyaniline–graphitic carbon nitride nanocomposite as a heterogeneous green catalyst for synthesis of indole-substituted 4H-chromenes. ACS Omega 3, 12163–12178.

Biswal, L., Nayak, S., Parida, K., 2021. Recent progress on strategies for the preparation of 2D/2D MXene/gC$_3$N$_4$ nanocomposites for photocatalytic energy and environmental applications. Catal. Sci. Technol. 11, 1222–1248.

Cao, S., Low, J., Yu, J., Jaroniec, M., 2015. Polymeric photocatalysts based on graphitic carbon nitride. Adv. Mater. 27, 2150–2176.

Cao, Y., Deng, Q., Liu, Z., Shen, D., Wang, T., Huang, Q., Du, S., Jiang, N., Lin, C.-T., Yu, J., 2017. Enhanced thermal properties of poly (vinylidene fluoride) composites with ultrathin nanosheets of MXene. RSC Adv. 7, 20494–20501.

Chaker, H., Chérif-Aouali, L., Khaoulani, S., Bengueddach, A., Fourmentin, S., 2016. Photocatalytic degradation of methyl orange and real wastewater by silver doped mesoporous TiO$_2$ catalysts. J. Photochem. Photobiol., A 318, 142–149.

Chen, L., Chen, C., Yang, Z., Li, S., Chu, C., Chen, B., 2021. Simultaneously tuning band structure and oxygen reduction pathway toward high-efficient photocatalytic hydrogen peroxide production using cyano-rich graphitic carbon nitride. Adv. Funct. Mater. 31, 2105731.

Chen, L., Zeng, X., Si, P., Chen, Y., Chi, Y., Kim, D.-H., Chen, G., 2014. Gold nanoparticle-graphite-like C$_3$N$_4$ nanosheet nanohybrids used for electrochemiluminescent immunosensor. Anal. Chem. 86, 4188–4195.

Cheng, L.-C., Huang, J.-H., Chen, H.M., Lai, T.-C., Yang, K.-Y., Liu, R.-S., Hsiao, M., Chen, C.-H., Her, L.-J., Tsai, D.P., 2012. Seedless, silver-induced synthesis of star-

shaped gold/silver bimetallic nanoparticles as high efficiency photothermal therapy reagent. J J. Mater. Chem. 22, 2244–2253.

Cheng, L., Zhang, D., Liao, Y., Li, F., Zhang, H., Xiang, Q., 2019. Constructing functionalized plasmonic gold/titanium dioxide nanosheets with small gold nanoparticles for efficient photocatalytic hydrogen evolution. J. Colloid Interface Sci. 555, 94–103.

Cheng, N., Tian, J., Liu, Q., Ge, C., Qusti, A.H., Asiri, A.M., Al-Youbi, A.O., Sun, X., 2013. Au-nanoparticle-loaded graphitic carbon nitride nanosheets: green photocatalytic synthesis and application toward the degradation of organic pollutants. ACS Appl. Mater. Interfaces 5, 6815–6819.

Choudhary, P., Kumar, A., Krishnan, V., 2021a. Nanoarchitectonics of phosphorylated graphitic carbon nitride for Sustainable, selective and Metal-free synthesis of primary amides. Chem. Eng. J. 431, 133695.

Choudhary, P., Sen, A., Kumar, A., Dhingra, S., Nagaraja, C., Krishnan, V., 2021b. Sulfonic acid functionalized graphitic carbon nitride as solid acid–base bifunctional catalyst for Knoevenagel condensation and multicomponent tandem reactions. Mater. Chem. Front. 5, 6265–6278.

Clavero, C., 2014. Plasmon-induced hot-electron generation at nanoparticle/metal-oxide interfaces for photovoltaic and photocatalytic devices. Nat. Photonics 8, 95.

Debow, S., Zhang, T., Liu, X., Song, F., Qian, Y., Han, J., Maleski, K., Zander, Z.B., Creasy, W.R., Kuhn, D.L., 2021. Charge dynamics in TiO$_2$/MXene composites. J. Phys. Chem. C 125, 10473–10482.

DeSario, P.A., Pietron, J.J., Brintlinger, T.H., McEntee, M., Parker, J.F., Baturina, O., Stroud, R.M., Rolison, D.R., 2017. Oxidation-stable plasmonic copper nanoparticles in photocatalytic TiO$_2$ nanoarchitectures. Nanoscale 9, 11720–11729.

Ding, X., Li, C., Wang, L., Feng, L., Han, D., Wang, W., 2019. Fabrication of hierarchical g-C$_3$N$_4$/MXene-AgNPs nanocomposites with enhanced photocatalytic performances. Mater. Lett. 247, 174–177.

Dong, F., Li, Y., Wang, Z., Ho, W.-K., 2015. Enhanced visible light photocatalytic activity and oxidation ability of porous graphene-like g-C$_3$N$_4$ nanosheets via thermal exfoliation. Appl. Surf. Sci. 358, 393–403.

Duoerkun, G., Zhang, Y., Shi, Z., Shen, X., Cao, W., Liu, T., Liu, J., Chen, Q., Zhang, L., 2020. Construction of n-TiO$_2$/p-Ag$_2$O junction on carbon fiber cloth with Vis–NIR photoresponse as a filter-membrane-shaped photocatalyst. Adv. Fiber Mater. 2, 13–23.

Feng, W., Luo, H., Wang, Y., Zeng, S., Tan, Y., Deng, L., Zhou, X., Zhang, H., Peng, S., 2019. Mxenes derived laminated and magnetic composites with excellent microwave absorbing performance. Sci. Rep. 9, 1–10.

Geng, G., Chen, P., Guan, B., Liu, Y., Yang, C., Wang, N., Liu, M., 2017. Sheetlike gold nanostructures/graphene oxide composites via a one-pot green fabrication protocol and their interesting two-stage catalytic behaviors. RSC Adv. 7, 51838–51846.

González-Mendoza, A.L., Cabrera-Lara, L.I., 2015. Reaction parameters for controlled sonosynthesis of gold nanoparticles. J. Mex. Chem. Soc. 59, 119–129.

Halim, J., Cook, K.M., Naguib, M., Eklund, P., Gogotsi, Y., Rosen, J., Barsoum, M.W., 2016. X-ray photoelectron spectroscopy of select multi-layered transition metal carbides (MXenes). Appl. Surf. Sci. 362, 406–417.

Hasija, V., Raizada, P., Sudhaik, A., Sharma, K., Kumar, A., Singh, P., Jonnalagadda, S.B., Thakur, V.K., 2019. Recent advances in noble metal free doped graphitic carbon nitride based nanohybrids for photocatalysis of organic contaminants in water: a review. Appl. Mater. Today 15, 494–524.

Jeong, S.Y., Shin, H.-M., Jo, Y.-R., Kim, Y.J., Kim, S., Lee, W.-J., Lee, G.J., Song, J., Moon, B.J., Seo, S., 2018. Plasmonic silver nanoparticle-impregnated nanocomposite BiVO$_4$ photoanode for plasmon-enhanced photocatalytic water splitting. J. Phys. Chem. C 122, 7088–7093.

Khan, M., Al-Oufi, M., Toseef, A., Nadeem, M., Idriss, H., 2018. Comparing the reaction rates of plasmonic (gold) and non-plasmonic (palladium) metal particles in photocatalytic hydrogen production. Catal. Lett. 148, 1–10.

Kumar, A., Choudhary, P., Kumar, A., Camargo, P.H., Krishnan, V., 2021a. Recent advances in plasmonic photocatalysis based on TiO$_2$ and noble metal nanoparticles for energy conversion, environmental remediation, and organic synthesis. Small 18, 2101638.

Kumar, A., Choudhary, P., Kumar, K., Kumar, A., Krishnan, V., 2021b. Plasmon induced hot electron generation in two dimensional carbonaceous nanosheets decorated with Au nanostars: enhanced photocatalytic activity under visible light. Mater. Chem. Front. 5, 1448–1467.

Kumar, A., Reddy, K.L., Kumar, S., Kumar, A., Sharma, V., Krishnan, V., 2018a. Rational design and development of lanthanide-doped NaYF4@ CdS–Au–RGO as quaternary plasmonic photocatalysts for harnessing visible–near-infrared broadband spectrum. ACS Appl. Mater. Interfaces 10, 15565–15581.

Kumar, S., Kumar, A., Kumar, A., Balaji, R., Krishnan, V., 2018b. Highly efficient visible light active 2D-2D nanocomposites of N-ZnO-g-C3N4 for photocatalytic degradation of diverse industrial pollutants. ChemistrySelect 3, 1919–1932.

Leng, F., Mai, W., Zhang, X., Liu, R., Lin, X., Huang, J., Lou, H., Xie, Y., Fu, R., Wu, D., 2018. Construction of functional nanonetwork-structured carbon nitride with Au nanoparticle yolks for highly efficient photocatalytic applications. Chem 54, 7159–7162.

Li, H., Zhang, L., 2017. Photocatalytic performance of different exposed crystal facets of BiOCl. Curr. Opin. Green Sustainable Chem. 6, 48–56.

Lin, B., Li, H., An, H., Hao, W., Wei, J., Dai, Y., Ma, C., Yang, G., 2018. Preparation of 2D/2D g-C$_3$N$_4$ nanosheet@ ZnIn$_2$S$_4$ nanoleaf heterojunctions with well-designed high-speed charge transfer nanochannels towards high-efficiency photocatalytic hydrogen evolution. Appl. Catal., B 220, 542–552.

Mishra, B.P., Parida, K., 2021. Orienting Z scheme charge transfer in graphitic carbon nitride-based systems for photocatalytic energy and environmental applications. J. Mater. Chem. 9, 10039–10080.

Mohan, H., Lim, J.M., Lee, S.W., Cho, M., Park, Y.J., Seralathan, K.K., Oh, B.T., 2020. V_2O_5/RGO/Pt nanocomposite on oxytetracycline degradation and pharmaceutical effluent detoxification. J. Chem. Technol. Biotechnol. 95, 297–307.

Mostafaloo, R., Mahmoudian, M.H., Asadi-Ghalhari, M., 2019. $BiFeO_3$/Magnetic nanocomposites for the photocatalytic degradation of cefixime from aqueous solutions under visible light. J. Photochem. Photobiol., A 382, 111926.

Nguyen, V.-H., Nguyen, B.-S., Hu, C., Nguyen, C.C., Nguyen, D.L.T., Nguyen Dinh, M.T., Vo, D.-V.N., Trinh, Q.T., Shokouhimehr, M., Hasani, A., 2020. Novel architecture titanium carbide ($Ti_3C_2T_x$) MXene cocatalysts toward photocatalytic hydrogen production: a mini-review. Nanomaterials 10, 602.

Pawar, G.S., Elikkottil, A., Pesala, B., Tahir, A.A., Mallick, T.K., 2019. Plasmonic nickel nanoparticles decorated on to LaFeO3 photocathode for enhanced solar hydrogen generation. Int. J. Hydrogen Energy 44, 578–586.

Pawar, R.C., Kang, S., Ahn, S.H., Lee, C.S., 2015. Gold nanoparticle modified graphitic carbon nitride/multi-walled carbon nanotube (gC_3N_4/CNTs/Au) hybrid photocatalysts for effective water splitting and degradation. RSC Adv. 5, 24281–24292.

Peng, C., Wei, P., Chen, X., Zhang, Y., Zhu, F., Cao, Y., Wang, H., Yu, H., Peng, F., 2018. A hydrothermal etching route to synthesis of 2D MXene (Ti_3C_2, Nb_2C): enhanced exfoliation and improved adsorption performance. Ceram. Int. 44, 18886–18893.

Qin, F.-X., Jia, S.-Y., Liu, Y., Li, H.-Y., Wu, S.-H., 2015. Adsorptive removal of bisphenol A from aqueous solution using metal-organic frameworks. Desalination Water Treat. 54, 93–102.

Rajender, G., Choudhury, B., Giri, P., 2017. In situ decoration of plasmonic Au nanoparticles on graphene quantum dots-graphitic carbon nitride hybrid and evaluation of its visible light photocatalytic performance. Nanotechnology 28, 395703.

Ran, J., Gao, G., Li, F.-T., Ma, T.-Y., Du, A., Qiao, S.-Z., 2017. Ti_3C_2 MXene co-catalyst on metal sulfide photo-absorbers for enhanced visible-light photocatalytic hydrogen production. Nat. Commun. 8, 1–10.

Salimi, M., Esrafili, A., Jafari, A.J., Gholami, M., Sobhi, H.R., Nourbakhsh, M., Akbari-Adergani, B., 2019. Photocatalytic degradation of cefixime with MIL-125 (Ti)-mixed linker decorated by $g-C_3N_4$ under solar driven light irradiation. Colloids Surf., A 582, 123874.

Shah, S., Habib, T., Gao, H., Gao, P., Sun, W., Green, M., Radovic, M., 2017. Template-free 3D titanium carbide ($Ti_3C_2T_x$) MXene particles crumpled by capillary forces. Chem 53, 400–403.

Song, M., Wu, Y., Zheng, G., Du, C., Su, Y., 2019. Junction of porous $g-C_3N_4$ with B_iVO_4 using Au as electron shuttle for cocatalyst-free robust photocatalytic hydrogen evolution. Appl. Surf. Sci. 498, 143808.

Su, T., Hood, Z.D., Naguib, M., Bai, L., Luo, S., Rouleau, C.M., Ivanov, I.N., Ji, H., Qin, Z., Wu, Z., 2019. 2D/2D heterojunction of Ti_3C_2/gC_3N_4 nanosheets for enhanced photocatalytic hydrogen evolution. Nanoscale 11, 8138–8149.

Sun, Y., Jin, D., Sun, Y., Meng, X., Gao, Y., Dall'Agnese, Y., Chen, G., Wang, X.-F., 2018. gC_3N_4/$Ti_3C_2T_x$ (MXenes) composite with oxidized surface groups for efficient photocatalytic hydrogen evolution. J. Mater. Chem. 6, 9124–9131.

Sun, Y., Mwandeje, J.B., Wangatia, L.M., Zabihi, F., Nedeljković, J., Yang, S., 2020. Enhanced photocatalytic performance of surface-modified TiO_2 nanofibers with rhodizonic acid. Adv. Fiber Mater. 2, 118–122.

Tan, L., Xu, J., Zhang, X., Hang, Z., Jia, Y., Wang, S., 2015. Synthesis of $g-C_3N_4$/CeO_2 nanocomposites with improved catalytic activity on the thermal decomposition of ammonium perchlorate. Appl. Surf. Sci. 356, 447–453.

Tang, G., Zhang, F., Huo, P., Zulfiqarc, S., Xu, J., Yan, Y., Tang, H., 2019. Constructing novel visible-light-driven ternary photocatalyst of AgBr nanoparticles decorated 2D/ 2D heterojunction of $g-C_3N_4$/BiOBr nanosheets with remarkably enhanced photocatalytic activity for water-treatment. Ceram. Int. 45, 19197–19205.

Tunc, I., Suzer, S., Correa-Duarte, M.A., Liz-Marzán, L.M., 2005. XPS characterization of Au (core)/SiO_2 (shell) nanoparticles. J. Phys. Chem. B 109, 7597–7600.

Wen, J., Xie, J., Chen, X., Li, X., 2017. A review on $g-C_3N_4$-based photocatalysts. Appl. Surf. Sci. 391, 72–123.

Wojciechowski, T., Rozmysłowska-Wojciechowska, A., Matyszczak, G., Wrzecionek, M., Olszyna, A., Peter, A., Mihaly-Cozmuta, A., Nicula, C., Mihaly-Cozmuta, L., Podsiadło, S., 2019. Ti_2C MXene modified with ceramic oxide and noble metal nanoparticles: synthesis, morphostructural properties, and high photocatalytic activity. Inorg. Chem. 58, 7602–7614.

Wu, S., Li, H., Li, X., He, H., Yang, C., 2018. Performances and mechanisms of efficient degradation of atrazine using peroxymonosulfate and ferrate as oxidants. Chem. Eng. J. 353, 533–541.

Xiang, Q., Li, F., Zhang, D., Liao, Y., Zhou, H., 2019. Plasma-based surface modification of $g-C_3N_4$ nanosheets for highly efficient photocatalytic hydrogen evolution. Appl. Surf. Sci. 495, 143520.

Xu, H., Xiao, R., Huang, J., Jiang, Y., Zhao, C., Yang, X., 2021. In situ construction of protonated $g-C_3N_4$/Ti_3C_2 MXene Schottky heterojunctions for efficient photocatalytic hydrogen production. Chin. J. Catal. 42, 107–114.

Yin, J., Zhan, F., Jiao, T., Wang, W., Zhang, G., Jiao, J., Jiang, G., Zhang, Q., Gu, J., Peng, Q., 2020. Facile preparation of self-assembled MXene@ Au@ CdS nanocomposite with enhanced photocatalytic hydrogen production activity. Sci. China Mater. 63, 2228–2238.

Zhang, T., Zhou, R., Wang, P., Mai-Prochnow, A., McConchie, R., Li, W., Zhou, R., Thompson, E.W., Ostrikov, K.K., Cullen, P.J., 2021. Degradation of cefixime antibiotic in water by atmospheric plasma bubbles: performance, degradation pathways and toxicity evaluation. Chem. Eng. J. 421, 127730.

Zhang, X.-Y., Li, H.-P., Cui, X.-L., Lin, Y., 2010. Graphene/TiO_2 nanocomposites: synthesis, characterization and application in hydrogen evolution from water photocatalytic splitting. J. Mater. Chem. 20, 2801–2806.

Zhao, C., Wang, Q., Zhang, H., Passerini, S., Qian, X., 2016. Two-dimensional titanium carbide/RGO composite for high-performance supercapacitors. ACS Appl. Mater. Interfaces 8, 15661–15667.

Zhu, J., Ha, E., Zhao, G., Zhou, Y., Huang, D., Yue, G., Hu, L., Sun, N., Wang, Y., Lee, L.Y. S., 2017. Recent advance in MXenes: a promising 2D material for catalysis, sensor and chemical adsorption. Coord. Chem. Rev. 352, 306–327.

Zhu, Z., Lu, Z., Wang, D., Tang, X., Yan, Y., Shi, W., Wang, Y., Gao, N., Yao, X., Dong, H., 2016. Construction of high-dispersed Ag/Fe_3O_4/$g-C_3N_4$ photocatalyst by selective photo-deposition and improved photocatalytic activity. Appl. Catal., B 182, 115–122.

Zinin, P.V., Ming, L.-C., Sharma, S.K., Khabashesku, V.N., Liu, X., Hong, S., Endo, S., Acosta, T., 2009. Ultraviolet and near-infrared Raman spectroscopy of graphitic C_3N_4 phase. Chem. Phys. Lett. 472, 69–73.